J Mater Sci (2024) 59:14639–14652

Metals & corrosion

Understanding crack growth within the γ' Fe_4N layer in a nitrided low carbon steel during monotonic and cyclic tensile testing

Rama Srinivas Varanasi[1,*], Motomichi Koyama[1,*], Mizuho Yokoi[1], Yusuke Ootani[1], Momoji Kubo[1], Kento Tanahara[2,3], and Osamu Umezawa[4]

[1] *Institute for Materials Research, Tohoku University, 2-1-1 Katahira, Aoba-ku, Sendai 980-8577, Japan*
[2] *Graduate School of Engineering, Yokohama National University, 79-5 Tokiwadai, Hodogaya, Yokohama 240-8501, Japan*
[3] *Present Address: Power Train Group, Manufacturing Engineering Development Center, Production Division, Komatsu Limited, 3-1-1 Ueno, Hirakata-city, Osaka 573-1011, Japan*
[4] *Faculty of Engineering, Yokohama National University, 79-5 Tokiwadai, Hodogaya, Yokohama 240-8501, Japan*

Received: 19 April 2024
Accepted: 14 July 2024
Published online: 28 July 2024

ABSTRACT

Nitriding is a cost-effective method to realize simultaneous improvements in tensile and fatigue properties and resistance to abrasion and corrosion. Previous studies reported that nitriding pure Fe enhances tensile strength by ~ 70% and fatigue limit by ~ 200%. It is due to the increase in surface hardness caused by the formation of $\gamma'(Fe_4N)$ and $\varepsilon(Fe_{2\text{-}3}N)$ nitrogen-containing intermetallic compound phases. However, the intermetallic compound layer is prone to brittle-like cracking. To better design nitrided steels, it is crucial to identify the crack growth mechanisms via analysis of the microstructural crack growth paths within the ~ 4–6 μm thick nitride layer. In the current work, we statistically evaluate the crack propagation behavior in the γ' Fe_4N layer during monotonic and cyclic tensile deformation in nitrided low-carbon steel (0.1 wt% C). Since nitriding typically results in the formation of columnar grains, the effect of morphology needs to be clarified. To this end, the steel was shot-peened and subsequently nitrided to promote equiaxed nitride grains morphology (~ 16% increase). Crack growth paths were comparatively evaluated for multiple cracks, and no significant effect of nitride morphology was observed. $\{100\}_{\gamma'}$ is the predominant transgranular crack path in the monotonic tensile tested specimen, followed by $\{111\}_{\gamma'}$. It is despite the elastic modulus of $\{111\}_{\gamma'} < \{100\}_{\gamma'}$. This contrary behavior is explained by $\{100\}_{\gamma'}$ plane having the lowest surface energy (density functional theory calculations). In the cyclic tensile loaded specimen, experiments revealed that transgranular cracking along $\{100\}_{\gamma'}$ (cracking via symmetric dislocation emission) or $\{111\}_{\gamma'}$ (slip plane cracking) is equally likely.

Handling Editor: Megumi Kawasaki.

Address correspondence to E-mail: rama.varanasi@tohoku.ac.jp; motomichi.koyama.c5@tohoku.ac.jp

https://doi.org/10.1007/s10853-024-10014-x

Springer

GRAPHICAL ABSTRACT

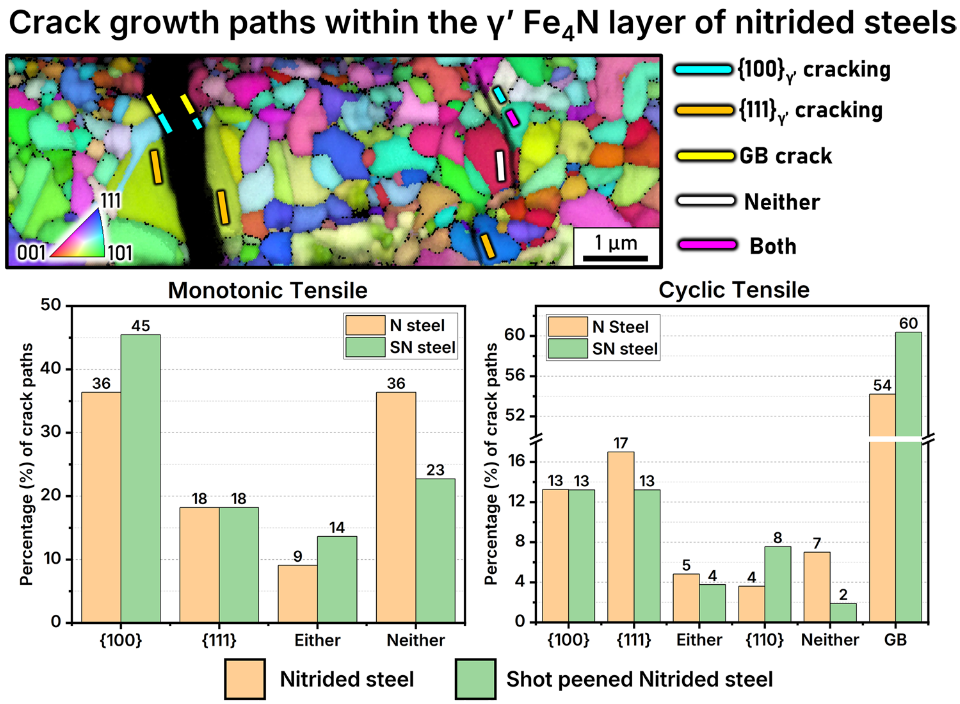

Introduction

Surface hardness is crucial for material life associated with metal fatigue and abrasion [1–3]. Fatigue life in steels is predominantly controlled by fatigue crack initiation at the surface and subsequent small crack growth in a microstructural scale (within 1 mm) [3–5]. Therefore, surface modifications by thermal and mechanical treatment have been attempted to improve the steel surface [6–8]. One of the most promising and cost-effective treatments is nitriding, which realizes simultaneous improvements in resistance to fatigue and abrasion owing to a significant increase in surface hardness [9, 10]. Earlier studies have reported that nitriding of pure Fe can enhance the ultimate tensile strength [11] and fatigue limit [12–14] (failure strength of 10^7 cycles) by ~ 70% and ~ 200%, respectively. The increase in surface hardness is owing to the formations of γ′ (Fe_4N) and ε ($Fe_{2\text{-}3}N$) nitrogen-containing intermetallic compound phases [15, 16].

Yet, there are some challenges in nitrided steels. Brittle-like tensile cracking occurs in the intermetallic compound layer or at its interface to the matrix when high stress is loaded [17, 18]. Furthermore, the pores arising from the degassing of nitrogen (due to the decomposition of iron-nitride phases into N_2 gas and Fe at higher temperatures) act as fatigue crack initiation sites [17, 19]. Therefore, in addition to crack initiation, fatigue crack growth behavior must also be controlled to endow robust resistance to fatigue. In particular, the small fatigue crack growth behavior in the thin nitride layer with a thickness of around 4–6 µm must be well understood. A crucial feature of the small fatigue crack growth is the microstructural growth path [20]. Specifically, the crystallographic information enables the identification of the crack growth mechanisms [21]. For instance, when crack growth via symmetrical dislocation emission at the crack tip, the crack growth path is mid-plane of the two symmetrical slip planes [22–25]. In addition, when a persistent slip at a crack tip causes crack growth, the crack growth path is the slip plane [25–27].

Previously, crack propagation behavior within the γ′ Fe_4N intermetallic compound layer in nitrided ultra-low carbon steel (0.008 wt% carbon) was reported [17, 18]. $\{100\}_{\gamma'}$ and $\{111\}_{\gamma'}$ planes were identified as the predominant crack growth paths in the monotonic and cyclic tests, respectively [17, 18]. While these are pioneering studies, the following critical aspects still need to be understood, which is the aim of the current work:

1. Steels designed for engineering applications typically contain carbon concentration ≥ 0.1 wt%, hence, the corresponding crack propagation behavior needs to be studied.
2. Since crack propagation occurs with a mixture of multiple growth mechanisms, statistical data of crystallographic crack paths is required for a deep understanding of the small crack growth behavior.
3. During nitriding, grain orientations with the fastest growth rates will grow preferentially, resulting in a columnar morphology [28]. The effect of such a morphology needs to be evaluated.
4. First-principles calculations by Takahashi et al. [29] demonstrated that in γ' Fe_4N, the elastic modulus of $\langle 111\rangle_{\gamma'}$ is the lowest, and that of $\langle 001\rangle_{\gamma'}$ is the highest. It suggests that the $\{111\}_{\gamma'}$ plane must be cracked when a cleavage fracture occurs. On the contrary, Koga et al. [17] reported $\{100\}_{\gamma'}$ cleavage during monotonic tensile testing in the nitrided ultra-low carbon steel. This paradox needs to be clarified.

In this study, we aim to understand the crack propagation behavior in the Fe_4N intermetallic compound layer of nitrided (N) low-carbon steel (0.1 wt% carbon). The statistical data of the crack growth paths induced by monotonic and cyclic tensile loading are comparatively examined through electron backscatter diffraction (EBSD) analysis for multiple cracks. To study the effect of nitride grain morphology on the crack growth mechanisms, shot peening and subsequent nitriding treatment (SN steel), which results in relatively fine grain size and equiaxed grain morphologies [30–33], are performed on the same low-carbon steel. Then, identical analyses are conducted in the nitrided layer of SN steel and compared to the specimen without shot peening (N steel).

Methods and materials

Materials and processing

The chemical composition of the low-carbon steel used is presented in Table 1. Both N and SN steels were annealed for 900 s at 1223 K. Annealing was followed by water quenching. Tensile specimens for monotonic and cyclic testing were cut along the rolling direction (RD). The tensile specimens have a gauge length of 30 mm, a width of 4 mm, and a thickness of 2 mm. Detailed sample dimensions have been provided elsewhere [17]. Shot peening was carried out in an air blast shot peening machine (Fuji Manufacturing). Soda-lime glass beads with 550 HV hardness and a mean diameter of 53 μm were used. Shot peening was performed at an injection pressure of 0.4 MPa with 200% coverage. Subsequently, the specimens were subjected to gas nitriding at 843 K for 18 ks (5 h) in an atmosphere of NH_3, N_2, and H_2. A nitriding potential (K_N) of 0.35 $Pa^{-0.5}$ was chosen based on the Leher diagram [19] to selectively generate the γ' nitride layer. Post nitriding at 843 K, the specimens were air-cooled (~ 19 K min^{-1}) to ambient conditions. The nitriding process is schematically depicted in Fig. 1.

Monotonic and cyclic tensile test

Both the monotonic and cyclic tensile loading experiments were conducted using a Shimadzu Autograph

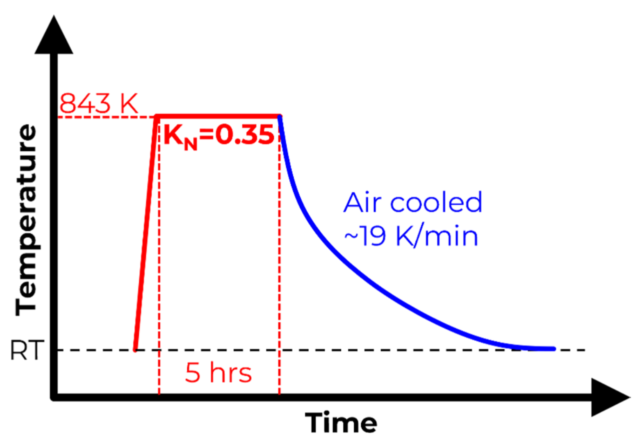

Figure 1 Schematic of the nitriding process to selectively generate the γ' nitride layer.

Table 1 Chemical composition of the low-carbon steel (weight %)

C	Si	Mn	P	S	Ni	Cr	Fe
0.1	0.19	0.34	0.0027	0.0022	0.05	0.12	Balance

AG-20KNIST machine. The tensile test was performed at a strain rate of $2.8 \times 10^{-4}\ s^{-1}$ (crosshead speed of 0.5 mm/min). Cyclic loading tests (force control) were performed with a triangular waveform under a stress rate of 1 kN s^{-1} and a stress ratio of 0.1. The maximum stress in the cyclic loading tests corresponds to the yield stress (measured from monotonic tensile stress) of N and SN steels, 563 MPa and 583 MPa, respectively. The cyclic tensile tests were interrupted after 10,000 cycles (no necking observed), and the microstructure was characterized.

Characterization

The cross-section (perpendicular to transverse direction-TD) was mechanically polished to perform EBSD and electron channeling contrast imaging (ECCI). The EBSD and ECCI studies were carried out in a Carl Zeiss Merlin field emission scanning electron microscope (FE-SEM) equipped with an EDAX Digiview 5 EBSD detector. Typically, defects such as dislocations and stacking faults appear with bright contrast in ECCI (when the grain is in channeling condition) [34]. EBSD data was analyzed using OIM Analysis 7 software, and only data points with confidence index value ≥ 0.1 were considered. The grain size was estimated from EBSD data using the intercept length method (edge grain included as half grains) over a width of 200 μm and 248 μm for N steel and SN steel, respectively. To assess the morphology of the Fe_4N grains, the grains are approximated to an ellipse; the grain is identified as equiaxed if the ratio of the minor axis to the major axis (aspect ratio) is > 0.4. Since the EBSD step size was 40 nm, only grains with grain size > 100 nm were considered for the aspect ratio analysis. No edge grains were considered for the aspect ratio analysis.

Density functional theory (DFT) calculations

The density functional theory (DFT) calculations were performed to obtain the surface energy of low-index planes in γ'-Fe_4N. Three surfaces were analyzed: (100), (110), and (111) surfaces. The surface energy was calculated by the following equation:

$$E_{surface} = \frac{E_{slab} - E_{bulk}}{2A}. \tag{1}$$

where $E_{surface}$, represents the surface energy per unit area. E_{slab} is the total energy of the slab model for a specific surface orientation, while E_{bulk}, corresponds to the total energy of the Fe_4N in its bulk phase. The term A denotes the surface area of the slab model. The calculation of surface state was performed with the slab model shown in Fig. 2. We employed the generalized

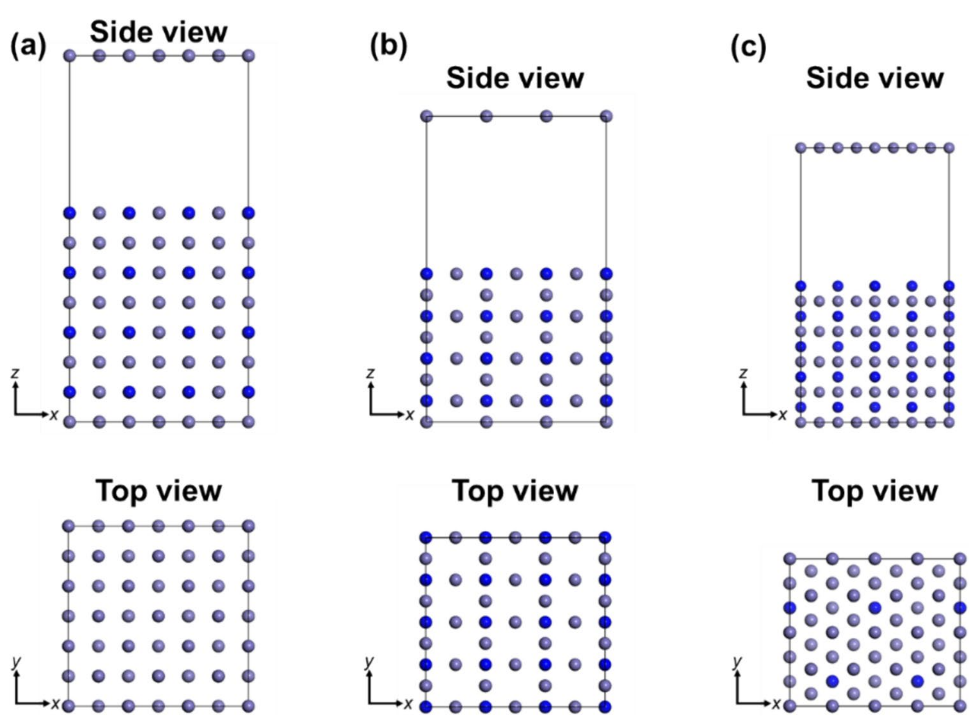

Figure 2 Slab models of Fe_4N **a** (100), **b** (110), and **c** (111) surfaces. The purple spheres represent iron (Fe) atoms, while the blue spheres indicate nitrogen (N) atoms.

gradient approximation type Perdew–Burke–Ernzerho (GGA-PBE) exchange–correlation functional, along with the DNP basis set and effective core potentials. Brillouin zone integrations were performed with the k-point at a grid spacing of < 0.05 $Å^{-1}$. All DFT calculations were performed with $DMol^3$ [35, 36].

Results and discussion

Initial microstructure: effect of shot peening

Table 2 summarizes the grain size, thickness, and morphology (percentage of equiaxed grains) of the Fe_4N layer in N and SN steels. The Fe_4N compound layer thickness (averaged over 32 regions using secondary electron imaging) for N and SN steels is 5.40 µm and 4.68 µm, respectively. This observation is contrary to the reports in the literature, wherein shot peening enhanced the nitride layer thickness owing to enhanced N diffusion due to grain refinement and plastic deformation at the surface [30, 32, 37]. However, understanding this phenomenon is beyond the scope of the present work.

Table 2 Grain size and morphology of the Fe_4N layer in N and SN steels

	Grain size (µm) (intercept length)	Equiaxed grains (area fraction %)	Compound layer thickness (µm)
N steel	0.412	60.7	5.40 ± 0.44
SN steel	0.318	76.8	4.68 ± 0.67

While negligible pores (or voids) were present in the compound layer in the N steel, a significant number of pores were observed close to the surface in the SN steel (Fig. 3). This observation contradicts the results of Kikuchi and Komotori [38], wherein they observed that pre-treatment of fine particle peening (FPP) suppressed the formation of pores in the compound layer. It was attributed to the FPP-induced depletion of Cr in the compound layer [38, 39]. However, the Cr concentration in the low-carbon steel investigated in the current work (Table 1) is significantly lower. Schwarz et al. [40] have observed that while pore formation was absent in single crystalline pure Fe, pores developed along grain boundaries in polycrystalline pure Fe and Fe-based binary alloys. Schwarz et al. [40] attributed the pore formation to grain boundaries acting as nucleation agents for N_2 gas-filled pores. Thus, it is likely that in the absence of significant Cr content, the grain refinement caused by shot peening promotes pore nucleation.

To ensure statistical robustness, grain size and morphology information (summarized in Table 2) of the nitride layer was extracted from 200 µm and 248 µm long EBSD scans for N and SN steel, respectively. Representative inverse pole figure (IPF) map of the γ'-Fe_4N layer for N and SN steel is shown in Fig. 4a, b, respectively. We observe two prominent effects of shot peening on the Fe_4N layer: (i) reduction in grain size and (ii) increase in the fraction of equiaxed grains. The reduction in Fe_4N grain size due to shot peening is consistent with earlier findings [32]. Previous studies demonstrated that for pure Fe, γ' Fe_4N_{1-x} initially nucleates at the Fe grain boundaries at the surface, subsequently growing laterally into the Fe grains [28,

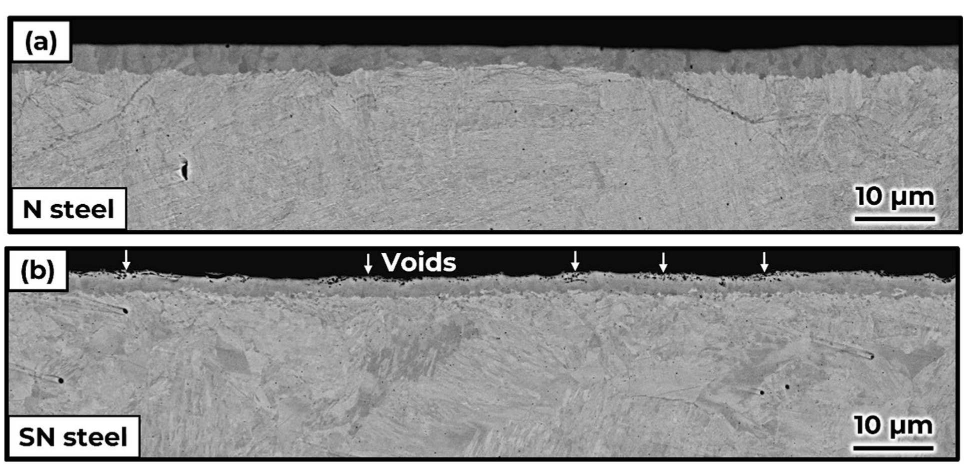

Figure 3 Enhanced void formation in the compound layer (close to the surface) of SN steel compared to N steel.

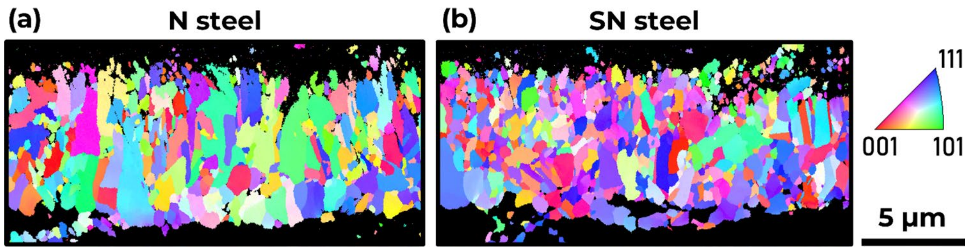

Figure 4 Representative inverse pole figure (IPF) maps of the γ'-Fe_4N layer for **a** N and **b** SN steel illustrating the decrease in grain size and increase in the formation of equiaxed grains in SN steel.

41]. Since shot peening results in grain refinement [30, 32, 37], the nucleation sites for γ' Fe_4N_{1-x} nitride would enhance, and the area available for lateral growth of the nucleated nitride would decrease. This results in both a reduction in grain size and the promotion of equiaxed morphology in the Fe_4N layer [28]. Competitive growth between nitride nanograins of different orientations occurs during the thickening of the nitride layer [28, 42]. Grains with orientations corresponding to the fastest growth rates will grow preferentially, resulting in a mixed morphology of columnar and equiaxed Fe_4N grains in the SN steel [28].

Crack propagation during monotonic tensile testing

Microstructural observations within the homogeneous deformation region (outside necking) post monotonic tensile fracture are shown in Figs. 5 and 6. ECC micrographs in Fig. 5a, a' indicate the columnar Fe_4N microstructure in N steel. Figures 5b, c and 6a–e show the EBSD analysis results of crack propagation paths during monotonic tensile testing in N and SN steels, respectively (evaluated from seven microcracks). We report the frequency of occurrence of each crystallographic crack path (Figs. 5c, 6e). Two

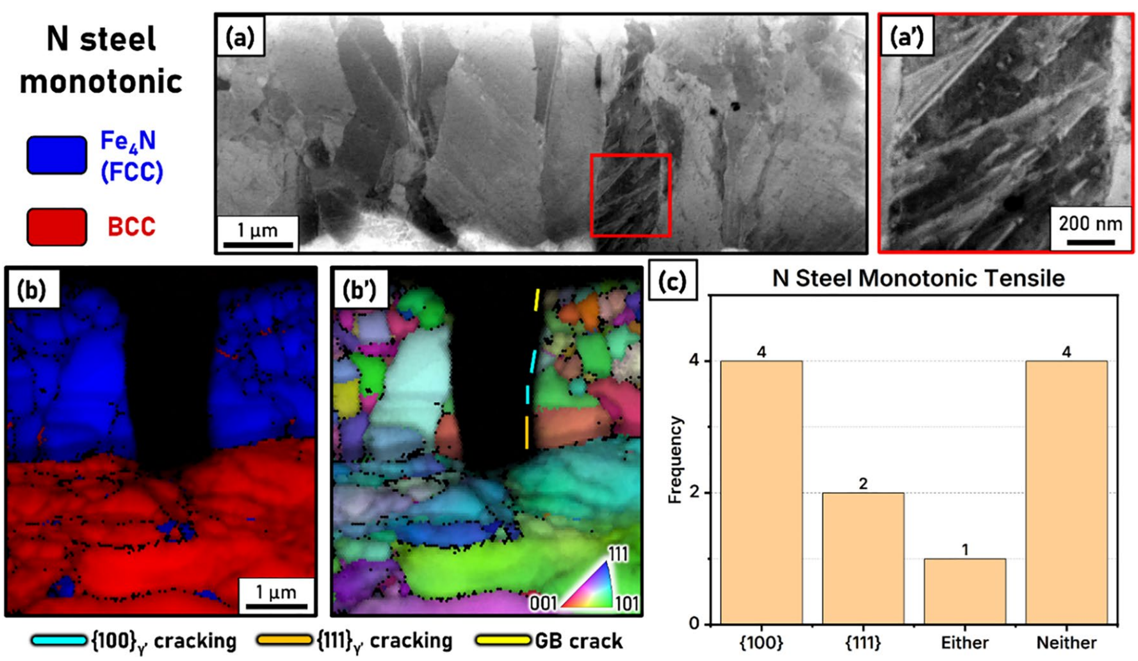

Figure 5 Microstructural observations in the homogeneous deformation region (outside necking) after monotonic tensile fracture. ECC micrographs illustrate the **a** columnar Fe_4N grains in the N steels, and **a'** the presence of dislocations and stacking faults formed during monotonic tensile testing. **b** Phase map and **b'** corresponding inverse pole figure (IPF) map around a microcrack formed in the N steel. **c** Frequency of occurrence of each crack path (seven microcracks were investigated).

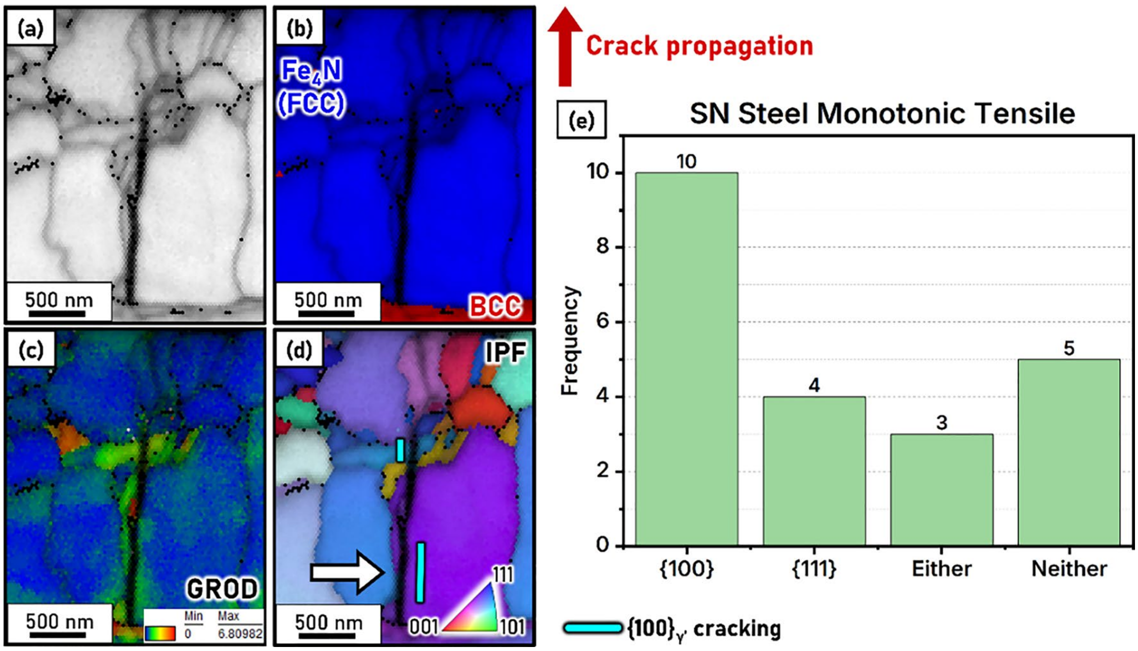

Figure 6 **a** Image quality map, **b** Phase map, **c** Grain reference orientation deviation (GROD) angle map, and **d** IPF map of a representative microcrack in the Fe_4N layer in the SN steel after monotonic loading. The white arrow indicates a crack propagating adjacent to the GB. **b** The frequency of occurrence of different crack paths (evaluated from EBSD studies on seven microcracks) .

transgranular γ'-Fe_4N cleavage planes are considered, namely $\{100\}_{\gamma'}$ and $\{111\}_{\gamma'}$ [17]. 'Neither' refers to the scenario wherein the transgranular crack does not correspond to either of the two planes (likely caused by the voids). Since the indexing of the crack path is based on two-dimensional EBSD trace analysis, there exist occasional cases wherein the trace of the cleavage plane corresponds to either of {100} and {111} planes (for instance, when the crack path is along $<0\bar{1}1>$). Such instances are labeled as 'Either.

Grain boundary (GB) has not been considered as a crack pathway for monotonic specimens. This is to avoid the overestimation of intergranular cracking. The width of the majority of the cracks investigated in monotonic tensile samples is ≥ 1 µm (Fig. 5a). Occasionally, we observed fine cracks in the monotonic tensile specimen wherein the width was ≤ 100 nm (possibly caused by the voids). For instance, a crack propagating towards the surface is shown in Fig. 6. A fine transgranular crack adjacent to a GB is highlighted with a white arrow in Fig. 6d. When the crack width is ~ 1 µm, a similar transgranular crack adjacent to a GB can be mis-indexed as intergranular cracking, causing an overestimation of GB cracking. It is due to the (i) preferential material removal at the edge during polishing and (ii) limited spatial resolution of EBSD (~ 30 nm) [43].

We observed that for both N steel and SN steel, the predominant transgranular crack path for the monotonic tensile specimen is $\{100\}_{\gamma'}$, followed by $\{111\}_{\gamma'}$ plane. Previously, Koga et al. [17] reported $\{100\}_{\gamma'}$ cleavage during monotonic tensile testing. Koga et al. [17] noted that it contradicts the elastic anisotropy results by Takahashi et al. [29] (E_{111} (lowest) $< E_{110} < E_{001}$, Table 3) that were obtained from first-principles calculations. Based on their experimental results, Koga et al. [17] concluded that E_{001} should be the lowest in γ'-Fe_4N and further inferred that the elastic modulus behavior of γ'-Fe_4N is identical to γ-Fe. In the current work, we propose an alternative explanation for $\{100\}_{\gamma'}$ cleavage that does not contradict the density functional theory (DFT) results of Takahashi et al. [29].

The fracture toughness (K_{IC}) of a brittle material in plane strain condition based on Griffith's theory is typically estimated by [46, 47]:

$$K_{IC} = \sqrt{\frac{2E\gamma_s}{1-v^2}} \quad (2)$$

Table 3 Summary of elastic anisotropy in plane normal direction, surface energies, Poisson's ratio, and fracture toughness (K_{IC}) for {100}, {111}, and {110} planes in γ-Fe and γ'-Fe_4N

	Plane	Elastic modulus in plane normal direction (GPa)		Surface energy (J m^{-2})		Poisson's ration	K_{IC} (MPa m$^{1/2}$)
γ-Fe	$\{100\}_\gamma$	103 (E_{001})	[29]	2.13	[44]	0.376 [45]	–
	$\{111\}_\gamma$	308 (E_{111})		2.08			
	$\{110\}_\gamma$	206 (E_{110})		2.15			
γ'-Fe_4N	$\{100\}_{\gamma'}$	230 (E_{001})	[29]	1.94	This work	0.36 (This work)	0.716
	$\{111\}_{\gamma'}$	127 (E_{111})		2.15			0.560
	$\{110\}_{\gamma'}$	143 (E_{110})		2.12			0.590

wherein E is Young's modulus in the plane normal direction to the cleavage plane, γ_s is the fracture surface energy of the cleavage plane, and v the Poisson's ratio. v for γ-Fe and γ'-Fe_4N is taken to be 0.376 [45] and 0.36 [29], respectively. It has to be noted that the elastic anisotropy of FCC γ'-Fe_4N is contrary to that of FCC Fe [29, 48]. The directional dependence of elastic modulus in Fe_4N and γ-Fe (FCC Fe–15 Cr–15 Ni) obtained from ab initio calculations by Takahashi et al. [29] is provided in Table 3. The surface energy of low-index surfaces in γ-Fe using DFT-based calculations was reported by Yu et al. [44] as shown in Table 3. However, similar data for the γ'-Fe_4N system was not available in the literature. To this end, we calculated the surface energies of low-index surfaces in γ'-Fe_4N using DFT ("Density functional theory (DFT) calculations" section). The surface energies follow $\gamma_s^{100} < \gamma_s^{110} < \gamma_s^{111}$. Based on Eq. 2, fracture toughness exhibits the opposite trend with $K_{IC}^{111} < K_{IC}^{110} < K_{IC}^{100}$.

It is important to note that Eq. 2 is only applicable for elastic materials that undergo brittle fracture. We observed the presence of dislocations and stacking faults in Fig. 5a' (which is consistent with previous report by Koga et al. [18]). Furthermore, the localized plastic deformation in the γ'-Fe_4N layer during crack propagation is evident from the grain reference orientation deviation (GROD) angle map [49], as shown in Fig. 6c. This indicates that the assumption that plasticity is absent is incorrect. Linear elastic fracture mechanics (LEFM) approximation (Eq. 2) is valid when the crack tip plastic zone is small compared to the crack length [50]. However, in the present scenario maximum possible crack length is < 6 μm (nitride layer thickness), further explaining the limitation of the LEFM approach. The preferred cleavage plane $\{100\}_{\gamma'}$ corresponds to the plane with lowest surface energy. Hence, it can be inferred that the cleavage during monotonic tensile testing is predominantly determined by the plane with lowest surface energy. It can be noted that in addition to $\{100\}_{\gamma'}$ cleavage, we also observe $\{111\}_{\gamma'}$ cracking which can be attributed to the lowest K_{IC}.

Crack propagation during cyclic tensile testing

Fatigue crack initiation in nitrided steels can involve the following mechanisms:

(i) Surface crack formation [51, 52].
(ii) Crack initiation at the interface of the compound layer and the base material due to the local heterogeneity caused by the difference in elastic modulus, hardness, and plastic deformation behaviour [53, 54].
(iii) Crack initiation at the pores/voids formed during nitriding [17, 55, 56].
(iv) Formation of fresh cracks ahead of a crack tip [57, 58].
(v) Sub-surface crack initiation at inclusions [59, 60].

However, the detailed statistical understanding of the crack initiation mechanisms is beyond the scope of the current work and constitutes future work.

Figure 7a–c show a discontinuous crack propagating towards the surface within the γ'-Fe_4N layer in an SN steel subject to cyclic tensile tests. The GROD angle map of the crack tip region shown in Fig. 7d demonstrates that the fatigue crack propagation involves plasticity evolution. This observation is consistent with previous transmission electron microscopy investigations of the γ'-Fe_4N layer after cyclic tests, which showed the crack propagation mechanism involved plastic deformation at the crack tip [18]. These results

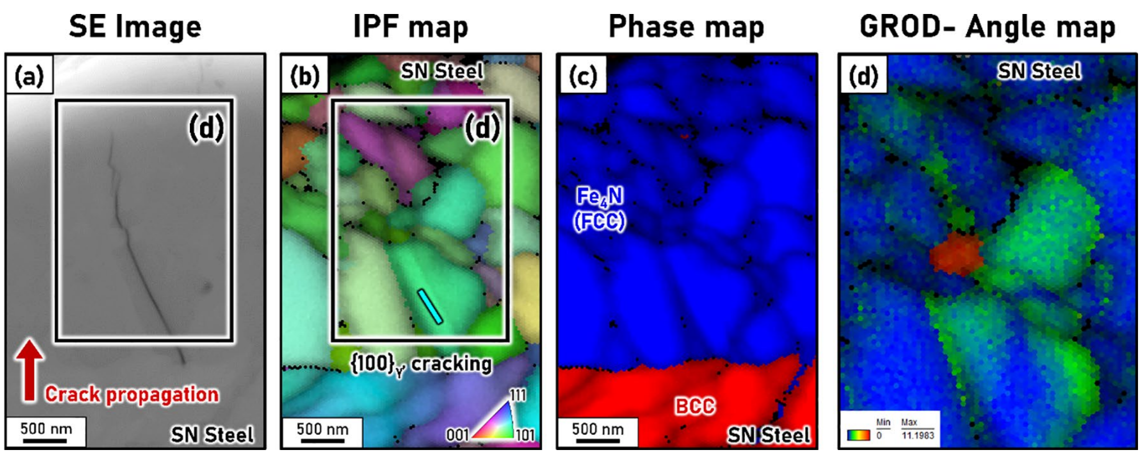

Figure 7 **a** Secondary electron (SE) image, **b** IPF map, **c** Phase map, and **d** Grain reference orientation deviation (GROD) angle map of a discontinuous microcrack within the Fe_4N layer in the SN steel after cyclic loading. Black boxes in **a**, **b** correspond to the GROD angle map in **d**.

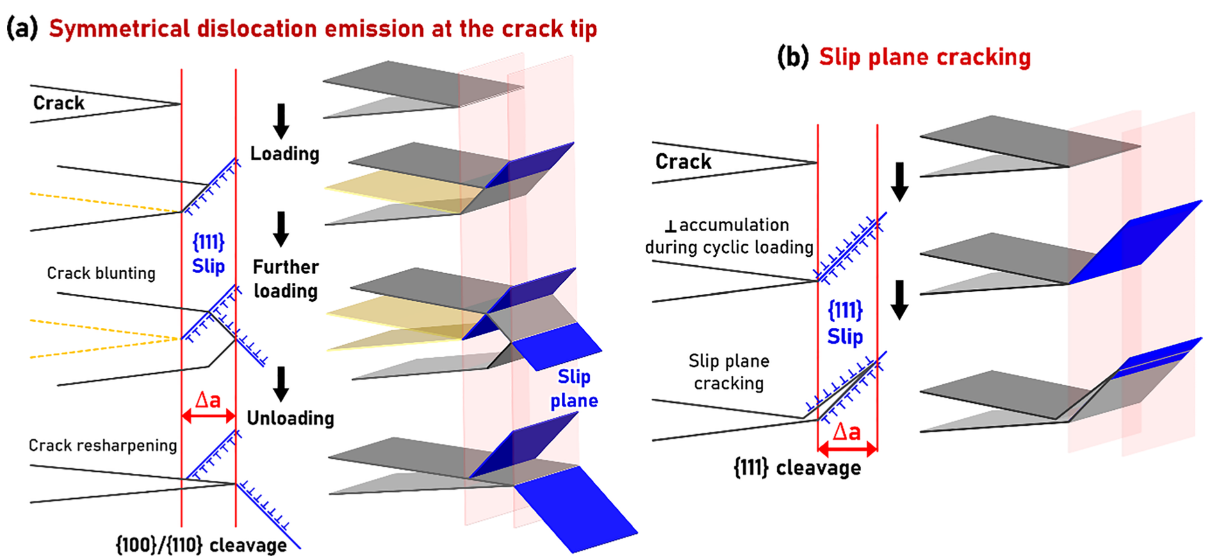

Figure 8 Schematic of fatigue crack propagation via **a** symmetrical dislocation emission at the crack tip and **b** slip plane cracking (adapted from Ju et al. [23]) in Fe_4N.

indicate that the crack propagation occurred via cyclic plasticity evolution at the crack tip.

When plasticity controls the fatigue crack growth, the crack growth is recognized to occur through two representative mechanisms. Figure 8a illustrates a schematic of fatigue crack propagation via symmetrical dislocation emission at the crack tip. The crack growth paths along $\{110\}_{\gamma'}$ and $\{100\}_{\gamma'}$ planes are the mid-plane of the two symmetrical $\{111\}_{\gamma'}$ slip planes [22–25]. The fatigue crack propagation on $\{111\}_{\gamma'}$ (Fig. 8b) is generally interpreted as slip plane cracking caused by persistent slip at a crack tip [25–27]. The crack propagation on the slip plane typically occurs when the crack length is smaller than the microstructure size, such as grain size.

The crack growth along $\{110\}_{\gamma'}$ and $\{100\}_{\gamma'}$ planes in Fig. 9a, c occurs via the symmetrical dislocation emission at the crack tip (Fig. 8a) [22–25]. The fatigue crack propagation occurs on $\{111\}_{\gamma'}$ (Fig. 9a, c) corresponds to the slip plane cracking mechanism (Fig. 8b) [25–27]. Figure 9d, e show the frequency of occurrence of crack paths after cyclic tensile testing in N steel

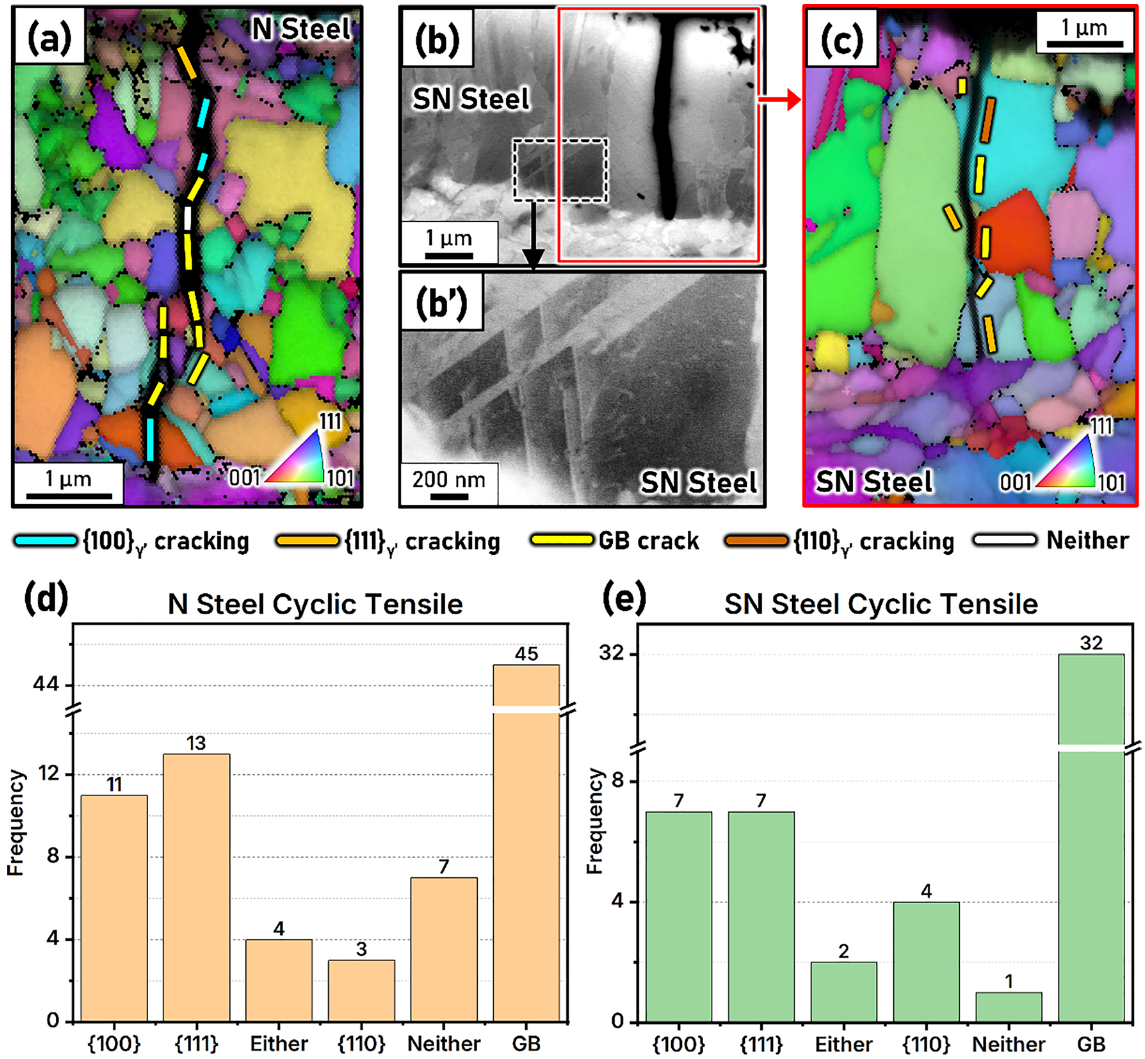

Figure 9 **a** Representative IPF map of crack propagation in cyclic testing in the N steel. **b** ECC micrograph of a microcrack in SN steel after cyclic tensile testing. (b') ECC micrograph at a higher magnification revealing the presence of stacking faults and dislocations (black box in **b**).The red box corresponds to the representative IPF map with various crack paths in **c**. **d** The frequency of occurrence of different crack paths in N steel after cyclic tensile loading (evaluated from EBSD studies on ten microcracks). **e** The frequency of occurrence of different crack paths in SN steel after cyclic loading (evaluated from EBSD studies on ten microcracks).

and SN steel, respectively. It is based on EBSD investigations of ten microcracks for each N and SN steel. 'Either' is a label for instances wherein the crack path could correspond to either $\{100\}_{\gamma'}$ or $\{111\}_{\gamma'}$. If the crack plane did not correlate to either of $\{100\}_{\gamma'}$ or $\{111\}_{\gamma'}$, we then checked for $\{110\}_{\gamma'}$ cracking. 'Neither' refers to the cases wherein the transgranular crack path does not match with any of the three planes ($\{100\}_{\gamma'}$, $\{111\}_{\gamma'}$, and $\{110\}_{\gamma}$). It is likely that a transgranular crack in the case of 'neither' is caused by the coalescence of discontinuous cracks and coalescence of cracks with pre-existing voids (due to localization of plasticity). Further in-situ and quasi-in-situ experimental investigations are required to verify this hypothesis.

For both N and SN steels, we observe that transgranular cracking along $\{100\}_{\gamma'}$ or $\{111\}_{\gamma'}$ plane is equally likely (Fig. 9d, e, Fig. 10). Since the width of fatigue cracks for the N and SN steel is ≤ 200 nm, we can index and report GB cracks with reasonable confidence (unlike monotonic testing). It can be noted that intergranular crack propagation is the predominant fatigue crack propagation pathway for both N and SN steels (Fig. 9d, e). As discussed in "Initial microstructure: effect of shot peening" section, Schwarz et al. [40]

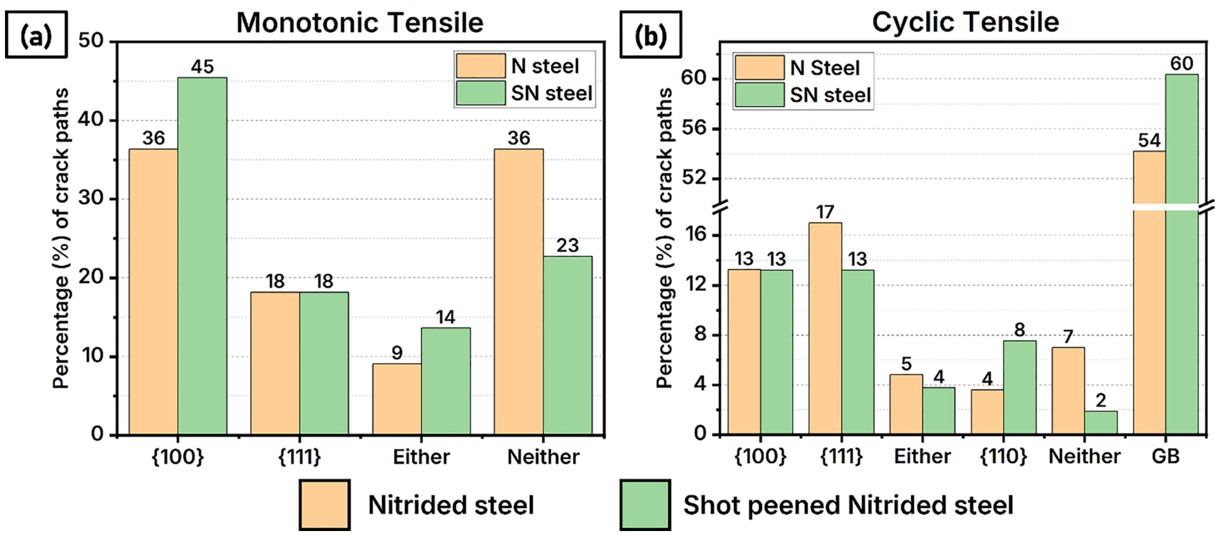

Figure 10 Summary of the statistical assessment of the cracking behavior in the γ' Fe_4N layer of N and SN steels during **a** monotonic and **b** cyclic tensile deformation.

reported that the grain boundaries act as nucleation sites for N_2 gas-filled pores. Thus, it is likely that such grain boundary void formation results in enhanced intergranular cracking. However, the effect of pre-existing voids on the crack growth pathways cannot be clarified via post-mortem investigations; it necessitates in-situ (or quasi-in-situ) studies and constitutes future work.

Conclusions

Figure 10 summarizes the statistical assessment of the cracking behavior in the γ' Fe_4N layer during monotonic and cyclic tensile deformation in a nitrided (N) and shot-peened and subsequently nitrided (SN) low-carbon steel. Crack growth paths were comparatively evaluated through EBSD analysis for multiple cracks.

1. SN steel consisted of ~ 16% more equiaxed nitride grains when compared to N steel. Additionally, enhanced void formation within the compound layer (near the surface) was observed in the SN steels. Since no considerable difference exists in the crack paths between N and SN steels, it is likely that the effect of nitride morphology and pores within the compound layer on the crack growth paths is negligible.
2. Both elastic modulus and LEFM-based fracture toughness of $\{111\}_{\gamma'}$ are lower when compared to $\{100\}_{\gamma'}$. However, $\{100\}_{\gamma'}$ is the predominant transgranular crack path in the monotonic tensile tested specimen, followed by $\{111\}_{\gamma'}$. This contrary behavior is explained by $\{100\}_{\gamma'}$ plane having the lowest surface energy (obtained from DFT calculations).
3. A predominant intergranular fracture was observed in the cyclic tensile loaded specimen. Experiments revealed that transgranular cracking along $\{100\}_{\gamma'}$ (cracking via symmetric dislocation emission) or $\{111\}_{\gamma'}$ (slip plane cracking) is equally likely.

A material's fatigue performance is dependent on both crack initiation and growth. This study presents a comprehensive understanding of the crack growth pathways. In addition, a statistical understanding of the crack initiation mechanisms is necessary to design nitrided steels. To this end, in-situ or quasi-in-situ experiments can help elucidate the role of microstructure on crack initiation. It is a topic of future work.

Acknowledgements

Authors gratefully acknowledge funding from Research Initiative of Structural Materials for Extreme Environment (RISME).

Declarations

Conflict of interest The authors declare that they have no known competing financial interests or personal relationships that could have appeared to influence the work reported in this paper.

References

[1] Sasahara H (2005) The effect on fatigue life of residual stress and surface hardness resulting from different cutting conditions of 0.45%C steel. Int J Mach Tools Manuf 45:131–136. https://doi.org/10.1016/j.ijmachtools.2004.08.002

[2] Hashemi B, RezaeeYazdi M, Azar V (2011) The wear and corrosion resistance of shot peened–nitrided 316L austenitic stainless steel. Mater Des 32:3287–3292. https://doi.org/10.1016/j.matdes.2011.02.037

[3] Chan KS (2010) Roles of microstructure in fatigue crack initiation. Int J Fatigue 32:1428–1447. https://doi.org/10.1016/j.ijfatigue.2009.10.005

[4] Ochi Y, Ishii A, Sasaki SK (1985) An experimental and statistical investigation of surface fatigue crack initiation and growth. Fatigue Fract Eng Mater Struct 8:327–339. https://doi.org/10.1111/j.1460-2695.1985.tb00431.x

[5] Mughrabi H (2002) On 'multi-stage' fatigue life diagrams and the relevant life-controlling mechanisms in ultrahigh-cycle fatigue. Fatigue Fract Eng Mater Struct 25:755–764. https://doi.org/10.1046/j.1460-2695.2002.00550.x

[6] Taylor D, Clancy OM (1991) The fatigue performance of machined surfaces. Fatigue Fract Eng Mater Struct 14:329–336. https://doi.org/10.1111/j.1460-2695.1991.tb00662.x

[7] Itoga H, Tokaji K, Nakajima M, Ko H-N (2003) Effect of surface roughness on step-wise S–N characteristics in high strength steel. Int J Fatigue 25:379–385. https://doi.org/10.1016/S0142-1123(02)00166-4

[8] Javidi A, Rieger U, Eichlseder W (2008) The effect of machining on the surface integrity and fatigue life. Int J Fatigue 30:2050–2055. https://doi.org/10.1016/j.ijfatigue.2008.01.005

[9] Limodin N, Verreman Y (2006) Fatigue strength improvement of a 4140 steel by gas nitriding: influence of notch severity. Mater Sci Eng A 435–436:460–467. https://doi.org/10.1016/j.msea.2006.07.034

[10] Hiraoka Y, Ishida A (2017) Effect of compound layer thickness composed of γ'-Fe_4N on rotated-bending fatigue strength in gas-nitrided JIS-SCM435 steel. Mater Trans 58:993–999. https://doi.org/10.2320/matertrans.M2017098

[11] Sun J, Tong WP, Zhang H, Du XD, Wu YC (2016) Enhanced strength and plasticity of gas nitrided iron by surface mechanical attrition pretreatment. Surf Coat Technol 286:279–284. https://doi.org/10.1016/j.surfcoat.2015.12.047

[12] Takeuchi S, Homma T (1958) Effect of shot peening on fatigue strength of metal, Effect on Polished State. The Research Institute for Iron, Steel and Other Metals. Tohoku University, Sendai

[13] Kim S, Yoon S, Kim J-H, Park S (2020) The effect of the transformation of ε-$Fe_{2\text{-}3}N$ into γ'-Fe_4N phase on the fatigue strength of gas-nitrided pure iron. Metals 10:823. https://doi.org/10.3390/met10060823

[14] Åman M, Wada K, Matsunaga H, Remes H, Marquis G (2020) The influence of interacting small defects on the fatigue limits of a pure iron and a bearing steel. Int J Fatigue 135:105560. https://doi.org/10.1016/j.ijfatigue.2020.105560

[15] Yamada Y, Hirohito E, Takahashi K (2019) Influence of crystal structure of nitride compound layer on torsion fatigue strength of alloy steel. Metals 9:1352. https://doi.org/10.3390/met9121352

[16] Mahboubi F, Samandi M, Dunne D, Bloyce A, Bell T (1995) Plasma nitriding of microalloyed steel. Surf Coat Technol 71:135–141. https://doi.org/10.1016/0257-8972(94)01012-8

[17] Koga N, Saito S, Umezawa O (2022) Crack initiation and propagation behavior in γ'-Fe_4N layer during monotonic and cyclic tensile deformation in the nitrided ultra-low carbon steel. J Mater Sci 57:2194–2207. https://doi.org/10.1007/s10853-021-06691-7

[18] Koga N, Tanahara K, Umezawa O (2022) Deformation structure around a crack in γ'-Fe_4N layer of nitrided extra-low-carbon steel subjected to cyclic tensile test. Metall Mater Trans A 53:1150–1155. https://doi.org/10.1007/s11661-022-06607-3

[19] Schneider RSE (2015) 9 - Austenitic nitriding and nitrocarburizing of steels. In: Mittemeijer EJ, Somers MAJ (eds) Thermochemical surface engineering of steels. Woodhead Publishing, Oxford, pp 373–400e. https://doi.org/10.1533/9780857096524.3.373

[20] Richards CE (1971) The influence of material properties on fatigue crack propagation as demonstrated by experiments on silicon iron. Acta Metall 19:583–596. https://doi.org/10.1016/0001-6160(71)90011-3

[21] Matsushita A, Ueki S, Mine Y, Takashima K (2021) Comparative study of microstructure-sensitive fatigue crack propagation in coarse- and fine-grained microstructures between stable and metastable austenitic stainless steels using miniature specimen. ISIJ Int 61:1688–1697. https://doi.org/10.2355/isijinternational.ISIJINT-2020-659

[22] Roth I, Kübbeler M, Krupp U, Christ H-J, Fritzen C-P (2010) Crack initiation and short crack growth in metastable austenitic stainless steel in the high cycle fatigue regime. Procedia Eng 2:941–948. https://doi.org/10.1016/j.proeng.2010.03.102

[23] Ju Y-B, Koyama M, Sawaguchi T, Tsuzaki K, Noguchi H (2017) Effects of ε-martensitic transformation on crack tip deformation, plastic damage accumulation, and slip plane cracking associated with low-cycle fatigue crack growth. Int J Fatigue 103:533–545. https://doi.org/10.1016/j.ijfatigue.2017.06.040

[24] Düber O, Künkler B, Krupp U, Christ H-J, Fritzen C-P (2006) Experimental characterization and two-dimensional simulation of short-crack propagation in an austenitic–ferritic duplex steel. Int J Fatigue 28:983–992. https://doi.org/10.1016/j.ijfatigue.2005.07.048

[25] Lynch SP (1981) Cleavage fracture in face-centred cubic metals. Metal Sci 15:463–468. https://doi.org/10.1179/msc.1981.15.10.463

[26] Zhang P, Zhang L, Baxevanakis KP, Lu S, Zhao LG, Bullough C (2021) Discrete crystal plasticity modelling of slip-controlled cyclic deformation and short crack growth under low cycle fatigue. Int J Fatigue 145:106095. https://doi.org/10.1016/j.ijfatigue.2020.106095

[27] Pineau A (2015) Crossing grain boundaries in metals by slip bands, cleavage and fatigue cracks. Philos Trans R Soc A: Math Phys Eng Sci 373:20140131. https://doi.org/10.1098/rsta.2014.0131

[28] Zhang C, Wen K, Gao Y (2023) Columnar and nanocrystalline combined microstructure of the nitrided layer by active screen plasma nitriding on surface-nanocrystalline titanium alloy. Appl Surf Sci 617:156614. https://doi.org/10.1016/j.apsusc.2023.156614

[29] Takahashi T, Burghaus J, Music D, Dronskowski R, Schneider JM (2012) Elastic properties of γ'-Fe_4N probed by nanoindentation and ab initio calculation. Acta Mater 60:2054–2060. https://doi.org/10.1016/j.actamat.2011.12.051

[30] Hassani-Gangaraj SM, Moridi A, Guagliano M, Ghidini A, Boniardi M (2014) The effect of nitriding, severe shot peening and their combination on the fatigue behavior and micro-structure of a low-alloy steel. Int J Fatigue 62:67–76. https://doi.org/10.1016/j.ijfatigue.2013.04.017

[31] Kovacı H, Hacısalihoğlu İ, Yetim AF, Çelik A (2019) Effects of shot peening pre-treatment and plasma nitriding parameters on the structural, mechanical and tribological properties of AISI 4140 low-alloy steel. Surf Coat Technol 358:256–265. https://doi.org/10.1016/j.surfcoat.2018.11.043

[32] Xu S, Cao Y, Duan B, Liu H, Wang J, Si C (2023) Enhanced strength and sliding wear properties of gas nitrided Ti–6Al–4V alloy by ultrasonic shot peening pre-treatment. Surf Coat Technol 458:129325. https://doi.org/10.1016/j.surfcoat.2023.129325

[33] Kikuchi S, Nakahara Y, Komotori J (2010) Fatigue properties of gas nitrided austenitic stainless steel pre-treated with fine particle peening. Int J Fatigue 32:403–410. https://doi.org/10.1016/j.ijfatigue.2009.07.019

[34] Zaefferer S, Elhami N-N (2014) Theory and application of electron channelling contrast imaging under controlled diffraction conditions. Acta Mater 75:20–50. https://doi.org/10.1016/j.actamat.2014.04.018

[35] Delley B (1990) An all-electron numerical method for solving the local density functional for polyatomic molecules. J Chem Phys 92:508–517. https://doi.org/10.1063/1.458452

[36] Delley B (2000) From molecules to solids with the DMol3 approach. J Chem Phys 113:7756–7764. https://doi.org/10.1063/1.1316015

[37] Manfridini APA, Godoy C, Avelar-Batista Wilson JC, Auad MV (2014) Surface hardening of IF steel by plasma nitriding: effect of a shot peening pre-treatment. Surf Coat Technol 260:168–178. https://doi.org/10.1016/j.surfcoat.2014.09.064

[38] Kikuchi S, Komotori J (2015) Evaluation of the gas nitriding of fine grained AISI 4135 steel treated with fine particle peening and its effect on the tribological properties. Mater Trans 56:556–562. https://doi.org/10.2320/matertrans.M2014448

[39] Hosmani SS, Schacherl RE, Mittemeijer EJ (2008) Compound layer formation on iron-based alloys upon nitriding; phase constitution and pore formation. HTM J Heat Treat Mater 63:139–146. https://doi.org/10.3139/105.100456

[40] Schwarz B, Göhring H, Meka SR, Schacherl RE, Mittemeijer EJ (2014) Pore formation upon nitriding iron and iron-based alloys: the role of alloying elements and grain boundaries. Metall Mater Trans A 45:6173–6186. https://doi.org/10.1007/s11661-014-2581-x

[41] Friehling PB, Poulsen FW, Somers MAJ (2001) Nucleation of iron nitrides during gaseous nitriding of iron; the effect of a preoxidation treatment. Z Met Mater Res Adv Tech 92:589–595
[42] Adamik M, Barna PB, Tomov I (1998) Columnar structures in polycrystalline thin films developed by competitive growth. Thin Solid Films 317:64–68. https://doi.org/10.1016/S0040-6090(97)00661-5
[43] Zaefferer S (2007) On the formation mechanisms, spatial resolution and intensity of backscatter Kikuchi patterns. Ultramicroscopy 107:254–266. https://doi.org/10.1016/j.ultramic.2006.08.007
[44] Yu J, Lin X, Wang J, Chen J, Huang W (2009) First-principles study of the relaxation and energy of bcc-Fe, fcc-Fe and AISI-304 stainless steel surfaces. Appl Surf Sci 255:9032–9039. https://doi.org/10.1016/j.apsusc.2009.06.087
[45] Kanhaiya K, Kim S, Im W, Heinz H (2021) Accurate simulation of surfaces and interfaces of ten FCC metals and steel using Lennard-Jones potentials. npj Comput Mater 7:1–15. https://doi.org/10.1038/s41524-020-00478-1
[46] Griffith AA (1921) VI. The phenomena of rupture and flow in solids. Phil Trans R Soc Lond A 221:163–198. https://doi.org/10.1098/rsta.1921.0006
[47] Yamasaki S, Morikawa T, Tanaka M, Watanabe Y, Yamashita M, Izumi S (2022) Evaluation of cleavage fracture behavior of C14 Fe_2W laves phase by first-principles calculations and crystal orientation analysis. ISIJ Int 62:2118–2125. https://doi.org/10.2355/isijinternational.ISIJINT-2022-122
[48] Gressmann T, Wohlschlögel M, Shang S, Welzel U, Leineweber A, Mittemeijer EJ, Liu Z-K (2007) Elastic anisotropy of γ'-Fe_4N and elastic grain interaction in γ'-Fe_4N_{1-y} layers on α-Fe: first-principles calculations and diffraction stress measurements. Acta Mater 55:5833–5843. https://doi.org/10.1016/j.actamat.2007.07.001
[49] Thomsen K, Mehnert K, Trimby PW, Gholinia A (2017) Quaternion-based disorientation coloring of orientation maps. Ultramicroscopy 182:62–67. https://doi.org/10.1016/j.ultramic.2017.06.021
[50] Suresh S, Ritchie RO (1984) Propagation of short fatigue cracks. Int Met Rev 29:445–475. https://doi.org/10.1179/imtr.1984.29.1.445
[51] Terent'ev VF, Michugina MS, Kolmakov AG, Kvedaras V, Čiuplys V, Čiuplys A, Vilys J (2007) The effect of nitriding on fatigue strength of structural alloys. Mechanics 64:12–22
[52] Yetim AF, Kovacı H, Uzun Y, Tekdir H, Çelik A (2023) A comprehensive study on the fatigue properties of duplex surface treated Ti6Al4V by plasma nitriding and DLC coating. Surf Coat Technol 458:129367. https://doi.org/10.1016/j.surfcoat.2023.129367
[53] Kovacı H, Yetim AF, Baran Ö, Çelik A (2016) Fatigue crack growth behavior of DLC coated AISI 4140 steel under constant and variable amplitude loading conditions. Surf Coat Technol 304:316–324. https://doi.org/10.1016/j.surfcoat.2016.07.045
[54] Bayrak Ö, Yetim AF, Alsaran A, Çelik A (2010) Fatigue life determination of plasma nitrided medical grade CoCrMo alloy. Fatigue Fract Eng Mater Struct 33:303–309. https://doi.org/10.1111/j.1460-2695.2010.01442.x
[55] Suh C-M, Hwang B-W, Murakami RI (2002) Characteristics of fatigue crack initiation and fatigue strength of nitrided lCr-lMo-02.5V turbine rotor steels. KSME Int J 16:1109–1116. https://doi.org/10.1007/BF02984021
[56] Ormastroni LMB (2022) Crack initiation mechanisms in very high cycle fatigue at high temperatures of nibased single crystal superalloys: transition from internal sites to the surface. PhD thesis, ISAE-ENSMA Ecole Nationale Supérieure de Mécanique et d'Aérotechique-Poitiers. https://theses.hal.science/tel-04042436/. Accessed 17 June 2024
[57] Ritchie RO (2011) The conflicts between strength and toughness. Nat Mater 10:817–822. https://doi.org/10.1038/nmat3115
[58] Ritchie RO (1988) Mechanisms of fatigue crack propagation in metals, ceramics and composites: role of crack tip shielding. Mater Sci Eng A 103:15–28. https://doi.org/10.1016/0025-5416(88)90547-2
[59] Genel K, Demirkol M, Çapa M (2000) Effect of ion nitriding on fatigue behaviour of AISI 4140 steel. Mater Sci Eng A 279:207–216. https://doi.org/10.1016/S0921-5093(99)00689-9
[60] Weidner A, Lippmann T, Biermann H (2017) Crack initiation in the very high cycle fatigue regime of nitrided 42CrMo4 steel. J Mater Res 32:4305–4316. https://doi.org/10.1557/jmr.2017.308